 CMES, vol.72, no.4, pp.247-272, 2011

Material Point Method with RBF Interpolation

Htike Htike[1], Wen Chen[1], Yan Gu[1] and Junjie Yang[1]

Abstract: This paper makes the first attempt to employ the Radial Basis Function (RBF) interpolation in the material point method (MPM), in which the shape function is based on RBF and polynomial function and satisfies the partition of unity and possesses Delta-function property. It is worthy of stressing that the RBF interpolation has the merit of high smoothness and is very accurate and can easily be applied to the MPM framework for mapping information between moving particles, known as material point in the MPM, and background grids. The RBF-based MPM is designed to overcome the unphysical results, such as shear stress distribution of the cantilever beam, in the traditional MPM with linear shape function. This study chooses the Mutiquadric (MQ) function as the RBF. The present strategy is tested to the benchmark cantilever beam and the circular disk impact problems. Numerical results are observed in good agreement with the analytical solutions and satisfy the conservation of energy.

Keywords: Material point method, radial basis function, multiquadric, interpolation, meshless, stress analysis.

1 Introduction

The material point method (MPM) [Sulsky, Chen, and Schreyer (1994); Sulsky, Zhou, and Schreyer (1995)] is an extension of the particle-in-cell method [Harlow (1964)] to solve the solid mechanics problems. The method discretizes the continuum body via the Lagrangian particles, i.e., material points, and the material information such as mass, volume, velocity, stress, strain, body force, and the external force is carried by these material points. The background grid is used to solve the weak-form of motion equation as the standard finite element method [Chen and Brannon (2002); Zhang, Sze and Ma (2006)]. The material information is projected from material points to the grid nodes via interpolation, and then the equation of motion is solved on these nodes. The results of position and velocity increments

[1] Centre for Numerical Simulation Software in Engineering and Sciences, Department of Engineering Mechanics, Hohai University, Nanjing 210098, China

are interpolated from grids to the material points and are updated. The background grid is used to carry the temporary information and is then discarded after updating the material point information. In this way, the MPM can solve the large deformation problems without troublesome remesh and is an attractive meshless technique [Ma and Zhang (2007)].

The application of MPM to a wide range of engineering problems can be accessed in the literature [Sulsky, Zhou and Schreyer (1995); Sulsky and Schreyer (1996); Bardenhagen and Brackbill (1998); Bardenhagen, Brackbill and Sulsky (2000); Bardenhagen, Guilkey, Roessig, Brackbill, Witzel and Foster (2001); Wieckowski (2003); Wieckowski (2004); Nairn (2003)]. In the traditional MPM, the element based interpolation function is of C^0 continuity and lack enough smoothness to accurately represent some physical quantities, especially in the internal forces when the material points cross the element boundaries. To overcome this weakness, Bardenhagen and Kober (2004) proposed the so-called generalized interpolation material point method (GIMP) which is derived from a variational form using a Petrov-Galerkin discretization scheme. The GIMP introduces a particle characteristic function and provides the C^1 continuity for mapping data between the material point and the background grid. The GIMP can greatly reduce the severe impact of grid-crossing material points that can lead to computational errors in the internal forces. But this strategy can not eliminate all such impact. Steffen, Kirby and Berzins (2008) investigated the errors in internal force due to the quadrature errors in the MPM and proposed the use of quadratic B-spline basis function to represent the solutions at grids and also analyzed the convergence behaviors. They also pointed out the development of collocation methods and nodal integration [Beissel and Belytschko (1996); Chen, Yoon and Wu (2002)] due to the difficulty of various quadrature schemes.

In recent years, the fast development of radial basis function (RBF) interpolation has attracted growing attention thanks to its inherent meshless and high-degree smoothness merits. Franke (1982) observed that the interpolation schemes based on RBF perform preferably among 30 or so interpolation approaches. The RBF has been widely implemented not only for interpolation but also for the direct solution of partial differential equations [Kansa (1990); Liu and Gu (2001); Wang, Liu and Lin (2002); Wang and Liu (2002); Chen and Tanaka (2002)]. In this study, we make the first attempt to employ RBF to represent physical quantity for the interpolating data between material points and background grids under the MPM framework. Since the RBF interpolation is meshless, we do not need element for data mapping. Thus, we can avoid the problems of the element based data mapping scheme in the traditional MPM. In addition, the interpolation function is constructed using a set of nodes within the local support domain which simplifies the formulation of shape

function and its derivatives. This study chooses Multiquadric (MQ) function as the radial basis function augmented with linear polynomial term to satisfy the unique approximation in interpolation [Golberg, Chen, Bowman and Power (1998)]. The effectiveness of the present strategy is tested to some benchmark solid mechanics problems.

The organization of the rest of this paper is as follows. Section 2 introduces the basic strategy of the material point method. And then Section 3 presents the linear shape function in the traditional MPM and the construction of shape function from the RBF-based interpolation, followed by the numerical results and discussions in Section 4. Finally, Section 5 will draw some conclusions based on the reported results.

2 Methodology

Without a loss of generality, we illustrate our scheme in its solution of the elasticity problem.

2.1 Discretization of Governing Equations

The standard conservation equations of mass and momentum govern the material motion with the updated Lagrangian formation.

$$\frac{d\rho}{dt} + \rho \nabla . v = 0, \tag{1}$$

$$\rho a = \nabla . \sigma + \rho b, \tag{2}$$

where $\rho = \rho(x,t)$ is the current density of mass, $v = v(x,t)$ the velocity, $a = a(x,t)$ the acceleration, $\sigma = \sigma(x,t)$ the Cauchy stress tensor, and $b = b(x,t)$ the specific body force. ∇ denotes the gradient operator. In addition, the constitutive equations and kinematic relations are also the complements to the above governing equations.

Initially, the domain of continuum body Ω is discretized into a set of material points where each material point p is defined at the centre of corresponding sub-domain Ω_p as shown in Fig. 1. To discretize the governing equation, the regularized mass density is represented by a sum of the mass of material points as

$$\rho = \sum_{p=1}^{N_p} m_p \delta \left(x - x_p^t\right), \tag{3}$$

where δ denotes the Dirac delta function with the unit of inverse volume, x_p^trepresents the vector of current material point position at instant t, N_p is the total number of material points in a continuum body, and the subscript p (where p=*1, 2,...* N_p)

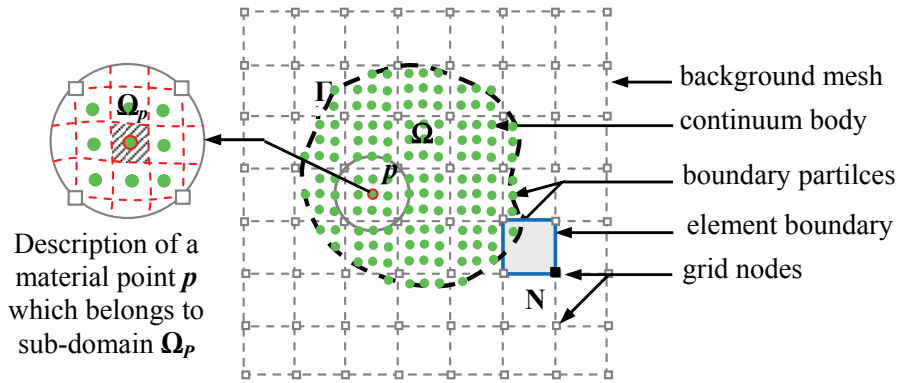

Figure 1: Descriptions of continuum body with a set of material points and the background mesh

refers to the material points. Moreover, m_p denotes the mass of a material point with the fixed amount for each time step, i.e, m_p is independent of time and the conservation of mass is thus automatically satisfied. To derive the weak form of the conservation of momentum, Eq. (2) is multiplied by the test function $\psi = \psi(x,t)$ and is then integrated over the physical domain Ω with boundary Γ

$$\int_\Omega \rho\psi.a\, d\Omega = \int_\Omega \psi\,.\nabla.\sigma d\Omega + \int_\Omega \rho\psi.\, b\, d\Omega. \tag{4}$$

By using the Green's divergence theorem, Eq.(4) can be written as

$$\int_\Omega \rho\psi.a\, d\Omega \;=\; -\int_\Omega \rho\sigma^s : \nabla\psi\, d\Omega \;+\; \int_{\Gamma^c} \psi.\tau\, d\Gamma \;+\; \int_\Omega \rho\psi.b\, d\Omega, \tag{5}$$

Γ^c is the part of the boundary Γ where the prescribed traction τ is applied. In Eq. (5), the vectors of specific stress $\sigma^s = \frac{\sigma}{\rho}$.

By applying the Dirac delta function's property and substituting Eq.(3) into Eq.(5), then the integral terms are converted to the sums of the quantities calculated at the material points on the current configuration

$$\sum_{p=1}^{N_p} m_p\, \psi_p^t\,.a_p^t = \; -\sum_{p=1}^{N_p} m_p \left(\sigma_p^{s,t} \;:\nabla\psi|_{x=x_p^t} - \;\psi_p^t.\, b_p^t\right) \;+\; \int_{\Gamma^c} \psi_p^t.\;\tau_p^t\, d\Gamma, \tag{6}$$

where$a_p^t = a\,\left(x_p^t,t\right)$, $b_p^t = b\,\left(x_p^t,t\right)$, $\psi_p^t = \psi\,\left(x_p^t,t\right)$, $\sigma_p^{s,t} = \sigma^s\left(x_p^t,t\right)$ and $\tau_p^t = \tau\,\left(x_p^t,t\right)$. And then the background grid is constructed to derive the discrete solution of balance of momentum equation at grid nodes. N_n represents the total

number of nodes on the background grid and the spatial coordinates of grid nodes are denoted as x_i, $i=1,2,\ldots N_n$. Then, the nodal basis function, referred to as shape function further below, is used to represent the current position of material points related to the nodal coordinates at instant t

$$x_p^t = \sum_{i=1}^{N_n} x_i^t \, N_{ip}^t, \tag{7}$$

where $N_{ip}^t = N_i\left(x_p^t\right)$ is the shape function. The velocity and acceleration of material points can be simply calculated by

$$v_p^t = \sum_{i=1}^{N_n} v_i^t \, N_{ip}^t, \tag{8}$$

$$a_p^t = \sum_{i=1}^{N_n} a_i^t \, N_{ip}^t. \tag{9}$$

v_i^t and a_i^t denote the nodal velocity and acceleration at instant t, respectively. Applying Eq. (7), Eq. (6) yields,

$$\sum_{i=1}^{N_n} \psi_i^t \cdot \sum_{p=1}^{N_p} \sum_{j=1}^{N_n} m_p N_{ip}^t N_{jp}^t a_j^t = \; - \sum_{i=1}^{N_n} \psi_i^t \cdot \sum_{p=1}^{N_p} m_p \, \sigma_p^{s,t} G_{ip}^t + \sum_{i=1}^{N_n} \psi_i^t \cdot \sum_{p=1}^{N_p} m_p b_p^t N_{ip}^t$$

$$+ \sum_{i=1}^{N_n} \psi_i^t \cdot \int_{\Gamma^c} N_{ip}^t \tau_p^t \, d\Gamma, \tag{10}$$

where $G_{ip}^t = \nabla N_i \,|_{x=x_p^t}$ is the spatial gradient of the shape function. The consistent mass matrixM_{ij}^t, the lumped nodal massM_i^t, the discrete specific traction τ_i^t and the specific body force b_i^t associated with the node i can be defined respectively by

$$M_{ij}^t = \sum_{p=1}^{N_p} m_p \, N_{ip}^t \, N_{jp}^t, \tag{11}$$

$$M_i^t = \sum_{p=1}^{N_p} m_p \, N_{ip}^t \, , \tag{12}$$

$$\tau_i^t \;\; = \int_{\Gamma^c} N_{ip}^t \, \tau_p^t \, d\Gamma, \tag{13}$$

$$b_i^t = \sum_{p=1}^{N_p} m_p \, b_p^t \, N_{ip}^t. \tag{14}$$

By applying arbitrary test function ψ_i^t and Eq. (11) – (14) to Eq. (10), then we have the simplest form of numerical solution at instant t

$$\sum_{j=1}^{N_n} M_{ij}^t \; a_j^t \; = \; -\sum_{p=1}^{N_p} m_p \; \sigma_p^{s,t} \; G_{ip}^t \; + \; b_i^t \; + \tau_i^t \; , \tag{15}$$

where the internal force vector is defined as

$$f_i^{t,int} = -\sum_{p=1}^{N_p} m_p \; \sigma_p^{s,t} \; G_{ip}^t \; , \tag{16}$$

and external force vector is

$$f_i^{t,ext} \; = \; b_i^t \; + \tau_i^t . \tag{17}$$

Finally, the weak form of the conservation of momentum equation is reduced to

$$\sum_{j=1}^{N_n} M_{ij}^t a_j^t \; = \; f_i^{t,int} \; + \; f_i^{t,ext} . \tag{18}$$

2.2 MPM Implementation Procedure

Here we introduce the general procedure of MPM which has little to do with particular shape function. And Section 3 will discuss the RBF-based shape function. Updating procedure on the stress values of material points plays a key role for the accuracy and efficiency. To analyze the energy conservation error in MPM, Bardenhagen (2002) considered the two cases, i.e., Updated Stress First (USF) and Updated Stress Last (USL), which depend on updated stress before and after the evaluation of internal force at the grid nodes, respectively. Buzzi, Pedroso and Giacomini (2008) also observed that the USF outperforms the USL in energy conservation. Below we give a general MPM implementation procedure of USF with the explicit time integration [Wallstedt and Guilkey(2008)].

At the initial time step, t= 0, the particle position (x_p), mass (m_p), velocity (v_p), deformation gradient(F_p), strain(ε_p), Cauchy stress (σ_p) and body force (b_p) must be recorded at the material points. For each time step we need to reset zero value of the nodal mass (M_i), momentum (q_i), rate of momentum($\dot{q}_i$), internal force $\left(f_i^{int}\right)$ and external force $\left(f_i^{ext}\right)$ associated with the node i. Hence, at the beginning of each time step, we discard the deformed background grid and compute the shape function based on the regenerated background grid and the current position of material points. After fulfilling these requirements, the detailed computational procedures in each time step can be described as follows:

Step1. Compute the nodal masses from the mass of the particles

$$M_i^t = \sum_{p=1}^{N_p} m_p \, N_{ip}^t \, . \tag{19}$$

Step2. Compute the nodal momentum from the mass and velocity of particles

$$q_i^t = \sum_{p=1}^{N_p} m_p \, v_p^t \, N_{ip}^t \ , \tag{20}$$

where $q_i^t = \sum_{j=1}^{N_n} M_{ij} \, v_j^t$ is associated with the consistent mass matrix and $q_i^t = M_i^t v_i^t$ is related to the lumped nodal mass.

Step3. Compute the nodal velocity using the lumped nodal mass $v_i^t = \frac{q_i^t}{M_i^t}$.

Step4. Compute the velocity gradient of material point from the nodal velocity

$$\nabla v_p^t = \sum_{i=1}^{N_n} G_{ip}^t \, v_i^t. \tag{21}$$

Step5. Compute the updated deformation gradient from the velocity gradient of material point

$$F_p^{t+\Delta t} = \left(\mathbf{I} + \nabla v_p^t . \Delta t\right) F_p^t, \tag{22}$$

where $\mathbf{I}$ is the identity tensor.

Step6. Compute the strain increment and the updated strain by

$$\Delta \varepsilon_p^t = \frac{\Delta t}{2} \sum_{i=1}^{N_n} \left(G_{ip}^t \, v_i^t + \left(G_{ip}^t v_i^t\right)^{\mathrm{T}} \right), \tag{23}$$

$$\varepsilon_p^{t+\Delta t} = \varepsilon_p^t + \Delta \varepsilon_p^t. \tag{24}$$

Step7. Compute the updated stress according to the constitutive model.

Step8. Computed the updated density from the updated deformation gradient

$$\rho_p^{t+\Delta t} = \frac{1}{J} \, \rho_p^0, \tag{25}$$

where $J = \left|F_p^{t+\Delta t}\right|$, and ρ_p^0 is the initial particle density at initial instant $t = 0$.

Step9. Compute the internal forces at nodes from the stresses of material points

$$f_i^{t,int} = -\sum_{p=1}^{N_p} m_p \, \sigma_p^{s,t} G_{ip}^t \quad . \tag{26}$$

Step10. Compute the external forces at nodes from the body force

$$f_i^{t,ext} = \sum_{p=1}^{N_p} m_p \, b_p^t \, N_{ip}^t. \tag{27}$$

The above representation Eq. (27) is based on the assumption that there are no tractions on a boundary of continuum body.

Step11. Compute the rate of momentum at the grid nodes

$$\dot{q}_i^t = f_i^{t,int} + f_i^{t,ext}, \tag{28}$$

where $\dot{q}_i^t = M_i^t \, a_i^t$ is called the rate of momentum.

Step12. Update the momentum from the rate of momentum at the grid nodes

$$q_i^{t+\Delta t} = q_i^t + \left(\dot{q}_i^t \, \Delta t \right). \tag{29}$$

Step13. Update the velocity of material points from the rate of nodal momentum

$$v_p^{t+\Delta t} = v_p^t + \sum_{i=1}^{N_n} \frac{\dot{q}_i^t \, N_{ip}^t \Delta t}{M_i}. \tag{30}$$

Step14. Update the position of material points from the nodal momentum

$$x_p^{t+\Delta t} = x_p^t + \sum_{i=1}^{N_n} \frac{q_i^{t+\Delta t} \, N_{ip}^t \Delta t}{M_i}. \tag{31}$$

Step15. At this step we have finished the evaluation cycle of this time step. And then we march to the next step by the time interval Δt and repeat all above-mentioned computational procedures from step 1 via the information of material points to initialize the nodal values on a new background grid.

The above-stated computational procedure calculates the information of material points via the nodal momentum instead of velocity following the suggestion of Sulsky, Zhou and Schreyer (1995). Namely, the numerical instability of acceleration usually arises at the boundary material points when they are moving into another element and are close to the element boundary with very few material points as

shown in Fig.1. The mass of grid node (**N**) evaluated by Eq. (12), has nearly zero value because of the small value of shape function. However, the internal force at that node (**N**) evaluated by Eq. (16), does not approach to zero because of the non-zero gradient of shape function. Therefore, the unphysical behaviour of nodal acceleration occurs on the outer nodes and leads to the separation of material points from the continuum body. For the application of lumped nodal mass, there is small amount of numerical dissipation [Burgess, Sulsky and Brackbill (1992)]. Ma, Giguere, Jayaraman and Zhang (2010) observed that the energy dissipation due to the lumped nodal mass can be overcome by using the diffusion coefficient. However, in most reports, the lumped nodal mass is still applied in order to simplify the computation. In this study, we also employ this approximation instead of using the mass matrix.

3 RBF interpolation in the MPM

In this section, we explain the mapping scheme applied in the traditional MPM and then describe the construction of shape function and its derivatives from the RBF interpolation.

3.1 Data mapping scheme in the traditional MPM

In the traditional MPM, the linear shape functions are derived via the Lagrangian interpolation based on the elements composed of a set of nodes. Mostly, 4-nodes quadrilateral elements in 2-D case as shown in Fig.2 and 2-nodes in 1-D case are used. The linear shape functions in 2-D case can be defined by using the local coordinates (ξ,η)

$$N_1(\xi,\eta) = \frac{1}{4}(1-\xi)(1-\eta), \tag{32}$$

$$N_2(\xi,\eta) = -\frac{1}{4}(1+\xi)(1-\eta), \tag{33}$$

$$N_3(\xi,\eta) = \frac{1}{4}(1+\xi)(1+\eta), \tag{34}$$

$$N_4(\xi,\eta) = -\frac{1}{4}(1+\xi)(1+\eta), \tag{35}$$

where $\xi = \frac{x-x_c}{a}$, $\eta = \frac{y-y_c}{b}$ and, $(x\,,\,y)$ and $(x_c\,,\,y_c)$ represent the spatial coordinate of corner nodes and the centre of the element, respectively.

As shown in Fig. 3, the gradient of shape functions is of discontinuity at the element boundary, and the traditional MPM suffers the computational error due to the requirement of C^1continuity in the calculation of material properties. To obtain the

representation of material quantities of higher smoothness, this study introduces the RBF-based shape function.

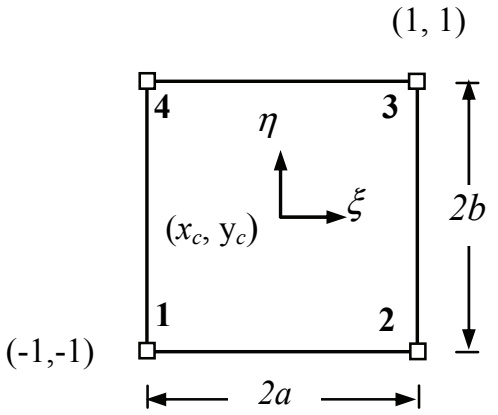

Figure 2: Depiction of element used in linear interpolation

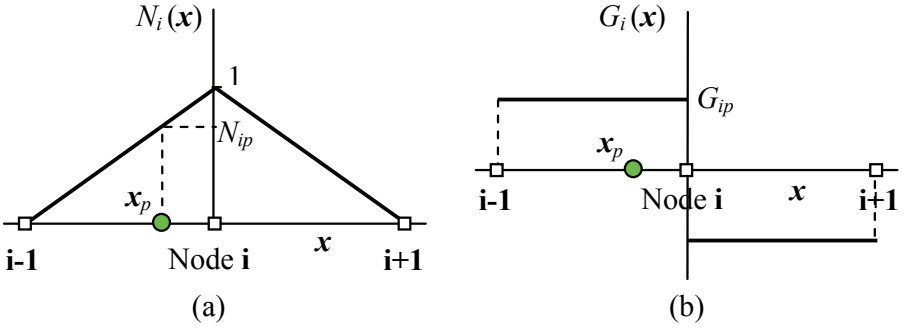

Figure 3: Depiction of (a) linear shape function and (b) gradient of linear shape function

3.2 Construction of shape function from RBF Interpolation

Liu and Gu (2001) proposed a point interpolation meshless method based on the radial basis functions and this method provides with accurate results for the simulation of solid mechanics problems [Wang, Liu and Lin (2002); Wang and Liu

(2002); Wang and Liu (2002)]. Partly inspired by their works and Franke's pioneering research on the RBF interpolation [Franke(1982)], the present study proposes the RBF- based shape function in the MPM framework. The RBF interpolation function $f(\mathbf{x})$ is constructed as

$$f(x) = \sum_{i=1}^{n} B(x)\ \alpha_i + \sum_{j=1}^{m} P_j(x)\ \beta_j$$

$$= \mathbf{B}^{\mathrm{T}}(x)\ \boldsymbol{\alpha} + \mathbf{P}^{\mathrm{T}}(x)\ \boldsymbol{\beta} = \begin{bmatrix}\mathbf{B}^{\mathrm{T}}(x) & \mathbf{P}^{\mathrm{T}}(x)\end{bmatrix} \begin{Bmatrix}\boldsymbol{\alpha}\\ \boldsymbol{\beta}\end{Bmatrix}, \tag{36}$$

where $B_i(\mathbf{x})$ is the radial basis function of choice and $P_j(\mathbf{x})$ is the polynomial basis functions. n denotes the number of nodes in a support domain of the point $\mathbf{x}$ of interest and $\mathbf{x}=(x,y)$ is the centre of supporting domain as shown in Fig.4 . m represents the number of polynomial terms, usually $m < n$. α_i and β_j are the coefficients of $B_i(\mathbf{x})$ and $P_j(\mathbf{x})$, respectively.

The radial basis function $B_i(\mathbf{x})$ has its basis variable of Euclidean distance r_i and

$$B_i(x) = B_i(r_i), \tag{37}$$

$$r_i = \sqrt{(x-x_i)^2 + (y-y_i)^2}, \tag{38}$$

where (x,y) and (x_i, y_i) are the spatial coordinates of the point interest and the grid node, respectively. This study chooses the multiquadric radial basis function (MQ RBF) because of its infinite smoothness and high accuracy in the function interpolation [Golberg, Chen, Bowman and Power (1998)]. The MQ is defined as

$$B_i(x) = \left(r_i^2 + R^2\right)^q, \tag{39}$$

where R and q are the parameters.

To evaluate the coefficients α_i and $\beta_j$in the interpolation expression of Eq. (36), interpolation is carried out by passing through the scattered nodal points within the support domain. The interpolation at the k^{th} node can be derived from Eq. (36) as

$$f_k(x) = f(x_k,y_k) = \sum_{i=1}^{n} B(x_k,y_k)\ \alpha_i + \sum_{j=1}^{m} P_j(x_k,y_k)\ \beta_j = \mathbf{B}_0^{\mathrm{T}}(x)\ \alpha + \mathbf{P}_0^{\mathrm{T}}(x)\ \beta, \tag{40}$$

where $k=1,2,\ldots,n$. And the following constraints on coefficient α_i are applied.

$$\sum_{i=1}^{n} P_j(x_i,y_i)\ \alpha_i = 0,\ j = 1,2,\ldots..,m. \tag{41}$$

By applying these constraints on Eq. (40), we have the following matrix form of the RBF interpolation

$$\begin{Bmatrix} \mathbf{f^e} \\ \mathbf{0} \end{Bmatrix} = \begin{bmatrix} \mathbf{B}_0 & \mathbf{P}_0 \\ \mathbf{P}_0^{\mathrm{T}} & \mathbf{0} \end{bmatrix} \begin{Bmatrix} \alpha \\ \beta \end{Bmatrix} = \mathbf{A} \begin{Bmatrix} \alpha \\ \beta \end{Bmatrix}, \tag{42}$$

where $\mathbf{f^e} = [f_1, f_2, ..., f_n]^{\mathrm{T}}$. The coefficients of the basis function can be calculated by

$$\begin{Bmatrix} \alpha \\ \beta \end{Bmatrix} = \mathbf{A}^{-1} \begin{Bmatrix} \mathbf{f^e} \\ \mathbf{0} \end{Bmatrix}. \tag{43}$$

By substituting Eq. (43) into Eq. (36), the interpolation functions can be simply expressed by

$$f(x) = \begin{bmatrix} \mathbf{B}^{\mathrm{T}}(x) & \mathbf{P}^{\mathrm{T}}(x) \end{bmatrix} \mathbf{A}^{-1} \begin{Bmatrix} \mathbf{f^e} \\ \mathbf{0} \end{Bmatrix} = \mathbf{N}(x)\, \mathbf{f^e}, \tag{44}$$

where **N**(**x**) is referred to the shape function. And then the general expression of the shape function of material point $\mathbf{x}_p$=(x_p, y_p) associated with the node k inside the support domain can be described as

$$\mathbf{N}_k(x_p) = \sum_{i=1}^{n} B_i(x_p)\, Z_{i,k} + \sum_{j=1}^{m} P_j(x_p)\, Z_{n+j,k}, \; k = 1,2,...n. \tag{45}$$

where $Z_{i,k}$ is the (i,k)element of matrix $\mathbf{A}^{-1}$. The gradient of shape functions can be derived as

$$\frac{\partial \mathbf{N}_k}{\partial x} = \sum_{i=1}^{n} \frac{\partial B_i}{\partial x} Z_{i,k} + \sum_{j=1}^{m} \frac{\partial P_j}{\partial x} Z_{n+j,k}, \tag{46}$$

$$\frac{\partial \mathbf{N}_k}{\partial y} = \sum_{i=1}^{n} \frac{\partial B_i}{\partial y} Z_{i,k} + \sum_{j=1}^{m} \frac{\partial P_j}{\partial y} Z_{n+j,k}. \tag{47}$$

The features of RBF- based shape function and its gradients are shown in Fig. 5 where we use the shape parameters of q= 0.5, R=1.0 and the 3 polynomial term.

3.3 Determination of parameters in RBF- based shape function

The requirements for the construction of RBF- based shape function can be described as follows:

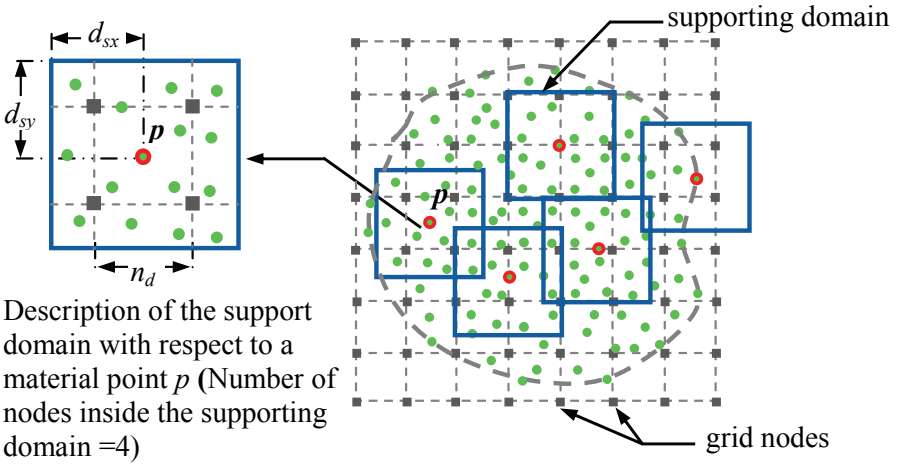

Description of the support domain with respect to a material point p (Number of nodes inside the supporting domain =4)

Figure 4: Description of material points with associated supporting domain

3.3.1 Determination of the support domain

The support domain is constructed by setting its centre on each material point as shown in Fig. 4. The square domain is selected as the shape of support domain for simplifying implementation. The scale of square support domain ($2d_{sx} \times 2d_{sy}$) is calculated from the relation of$d_{sx} = d_{sy} = d_s = \chi_s n_d$. Where χ_s is the dimensionless coefficient and n_d is the distance between two adjacent nodes. In this paper, the background grid is constructed with uniformly distributed nodes and the value of n_d in x and y direction is the same.

3.3.2 Determination of the shape parameters in RBF

The MQ RBF, which consists of two dimensionless shape parameters of R and q, is used to construct the shape function. Wang and Liu (2002) observed that the optimal parameter values of q=1.03 and R of around 1.42 for MQ basis in 2-D meshless calculation and this study also refers to these values for the choice of shape parameters in the computation of numerical examples presented in Section 4.

4 Numerical results and discussions

4.1 Cantilever beam problem

The 2-D classical benchmark cantilever beam problem is used to test the proposed technique. The accuracy of numerical results is checked by comparing with the

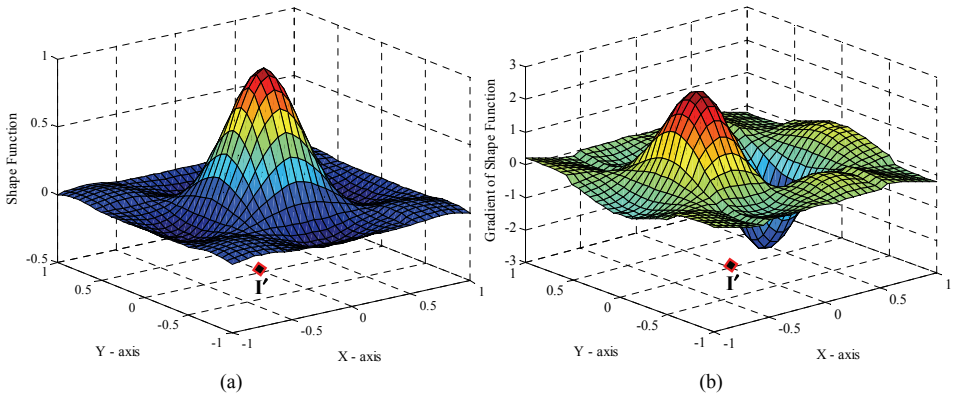

Figure 5: Description of RBF based: (a) Shape function $\mathbf{N}_{I'p}$ and (b) Gradient of shape function $\mathbf{G}_{I'p}$, for the material points with respect to node $\mathbf{I}\prime$

analytical solutions of deflection and stress distribution in a beam with rectangular cross section. The beam specifications including the material properties are as: length(L)=8, depth(D)=1, width(B)=1,Young's modulus(E)=3x10^7, Poison's ratio(υ)=0 and density (ρ=1000). For the consideration of infinitesimal deformation, the force (P=100) is applied at the rightmost end of the beam. The stress distribution in the beam is computed via the constitutive model of plane stress deformation stated as

$$\sigma_p^{t+\Delta t} = \sigma_p^t + \left[\frac{E}{1+\upsilon} \left\{ \Delta\varepsilon_p^t + \frac{\upsilon}{1-\upsilon} \, trace \, \left(\Delta\varepsilon_p^t\right) \, \mathbf{I} \right\} \right]. \tag{48}$$

The analytical solutions of the displacements in x and y directions [Timoshenko and Goodier (1970)] are defined as

$$u_x = \frac{\mathrm{P}\, y}{6EI} \left[(6L-3x)\, x + (2+\upsilon) \left(y^2 - \frac{D^2}{4} \right) \right], \tag{49}$$

$$u_y = -\frac{\mathrm{P}\, y}{6EI} \left[3\upsilon\, y^2 (L-x) + (4+5\upsilon) \frac{D^2 x}{4} + (3L-x)\, x^2 \right], \tag{50}$$

where $I = \frac{BD^3}{12}$ is the moment of inertia. And the corresponding stresses formulations are defined by

$$\sigma_x = \frac{\mathrm{P}\,(L-x)\, y}{I}\,,\ \sigma_y \approx 0\,,\ \tau_{xy} = -\frac{\mathrm{P}}{2\,I} \left[\frac{D^2}{4} - y^2 \right]. \tag{51}$$

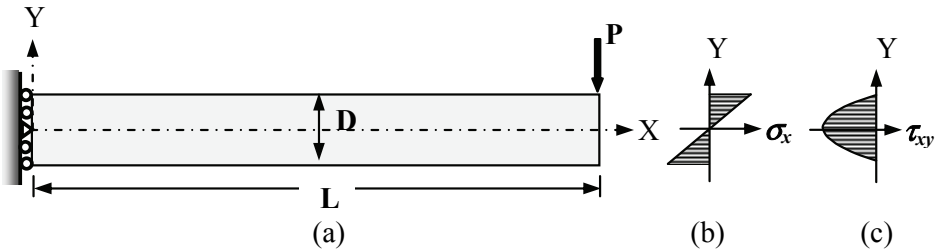

Figure 6: Depiction of: (a) a cantilever beam (b) normal stress distribution and (c) shear stress distribution

In theory, the behavior of stress distributions is shown in Fig.6.

For the numerical simulation, the beam is discretized by the uniformly distributed material points and mapped onto the background grid, which is created with 2-D quadrilateral elements. The force is applied as a parabolic variation of exterior acceleration on the rightmost boundary material points. To satisfy that condition, the shear stress field formulation is applied to transform the total force into the parabolic distribution of forces acting on those material points. For the boundary condition at the fixed support, the displacements in x and y directions of the node at the origin are set to be zero, and the displacement of other nodes are prevented only in the x direction as shown in Fig.7.

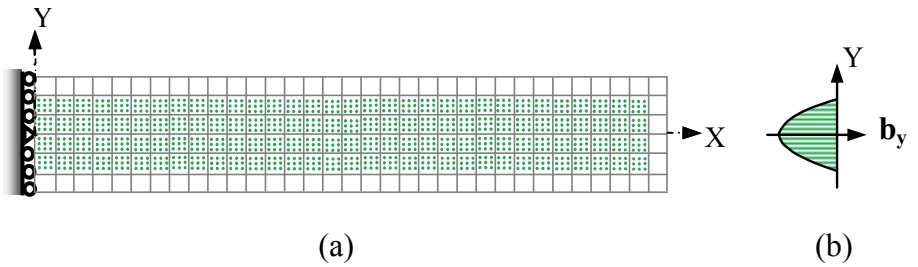

Figure 7: (a) The discrsetization for a cantilever beam and (b) distribution of forces on the rightmost boundary material points

In accordance with the quasi-static process, the exerting force is gradually increased at each time step until the total force reaches up to P=100. Time step (Δt=0.001 sec) and the total time taken for the loading process (T= 20 sec) is presumed. The total number of nodes on the background grid (N_n) varies 90 to 238 to 450 corresponding

to 288, 512 and 1152 material points (N_p) in the continuum body of beam.

For the parameters of MQ RBF- based shape function, the size of square support domain is fixed by χ_s= 2 and the shape parameter of q=1.03 is used. Another shape parameter $R$is around 1.42 and the polynomial term (m=3) is used to solve the cantilever beam problem. The relative error of the deflection is computed via the analytical and numerical deflection of overall material points as

$$\text{Rerr}_{\text{def}} = \frac{\sum_{p=1}^{N_p} \left|(\text{num\_def}_p - \text{anal\_def}_p)\right|}{\sum_{p=1}^{N_p} \left|\text{anal\_def}_p\right|} \times 100\ \%, \tag{52}$$

and, relative error of strain energy is computed as

$$\text{Rerr}_{\text{e}} = \frac{\left[\frac{1}{2}\sum_{p=1}^{N_p} \text{V}_p \left(\varepsilon_p^{\text{num}} - \varepsilon_p^{\text{anal}}\right) : \left(\sigma_p^{\text{num}} - \sigma_p^{\text{anal}}\right)\right]^{1/2}}{\left[\frac{1}{2}\sum_{p=1}^{N_p} \text{V}_p \left(\varepsilon_p^{\text{anal}} : \sigma_p^{\text{anal}}\right)\right]^{1/2}}, \tag{53}$$

where V_p is the volume of material point and the notations of "num" and "anal" refer to the numerical and analytical solutions, respectively.

The relative errors of deflection and strain energy are computed by considering the effect of shape parameters (q and R) and the nodal density value i.e. the total number of nodes included in the background grid. It is occurred that when the nodal density is increased, the computation process is broken down with the application of smaller R value and we can not calculate the error values as shown in Tab. 1. There may be a question concerning with the relation between the nodal density and the limitation of parameter R. In Fig.8, it shows the effect of nodal density and the parameter R on the estimation of relative errors.

Table 1: Relative error of deflection and strain energy

q=1.03	(N_n= 90,N_p=288)		(N_n= 238,N_p=512)		(N_n= 450,N_p=1152)	
	Rerr_{def}	Rerr_{e}	Rerr_{def}	Rerr_{e}	Rerr_{def}	Rerr_{e}
R =0.50	3.183	$1.019\text{x}10^{-1}$	1.419	$4.444\ \text{x}10^{-2}$	-	-
R =0.75	3.014	$8.127\ \text{x}10^{-2}$	0.657	$3.454\text{x}10^{-2}$	-	-
R =1.00	2.864	$6.816\text{x}10^{-2}$	0.395	$3.139\ \text{x}10^{-2}$	0.286	$2.645\ \text{x}10^{-2}$
R =1.25	2.790	$6.102\text{x}10^{-2}$	0.279	$3.062\text{x}10^{-2}$	0.272	$2.691\text{x}10^{-2}$

From Fig. 8(a), it is observed that the relative errors of deflection decrease with increasing nodal density for the smaller parameter value of R. When R value approaches to 2, the relative deflection error tends to increase with increasing nodal density values. If R value is selected around 1.25, then the relative error of deflection is almost the same for the higher nodal density value.

The relative error of strain energy is also examined to investigate convergence. As shown in Fig. 8(b), the relative energy errors decrease with the higher nodal density value. For the smaller nodal density, we can see differences between the relative strain energy errors for the different parameter values of R. However, for the higher nodal density value, the errors keep the same irrespective of the R value. Therefore, it can be understood that, for the higher nodal density, the numerical solution is insensitive with the shape parameter R within the range of 1∼1.5. Accordingly, the shape parameter q=1.03, and R=1.25 are selected in this study.

Fig. 9 shows the distribution of shear stress and normal stress at x=3.96, nearby the centre of longitudinal axis of the beam Then average deflections along the x-axis are illustrated in Fig. 10. 1152 grid nodes with 450 material points are used in the numerical simulations. It is evidenced that both numerical solutions obtained by the MPM with RBF interpolation are in good agreement with the analytical solutions.

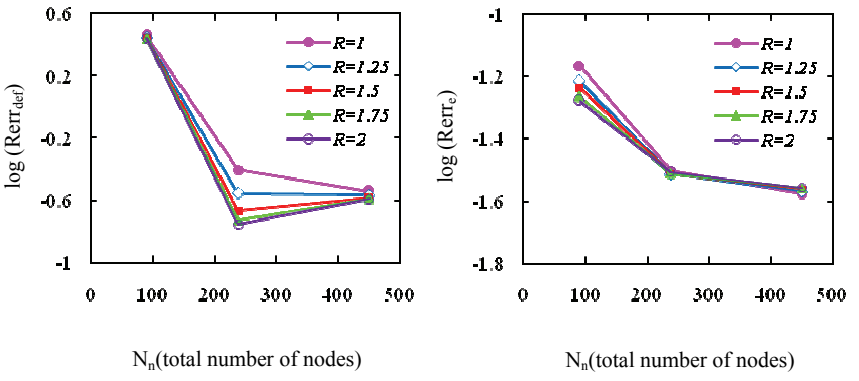

(a) (b)

Figure 8: Relative error distribution of (a) deflection and (b) strain energy values related with the nodal densities and shape parameter R (where, q=1.03)

The traditional MPM with linear interpolation can calculate accurate normal stress as shown in Fig. 12. However, it is stressed that the MPM with linear or quadratic element based interpolation function is impossible to obtain the good accuracy in the computation of shear stress distribution of the cantilever beam problem as

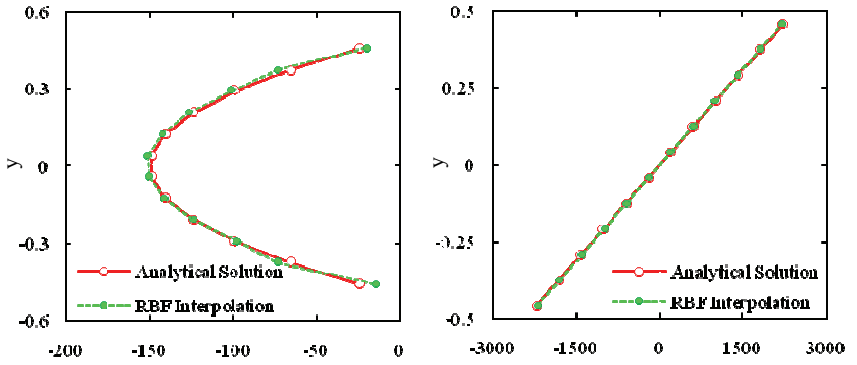

(a) Shear Stress (b) Normal Stress

Figure 9: Comparison of (a) shear stress and (b) normal stress distribution @x=3.96(near the centre of x- axis) (where q=1.03, R=1.25, N_n=450, N_p=1152)

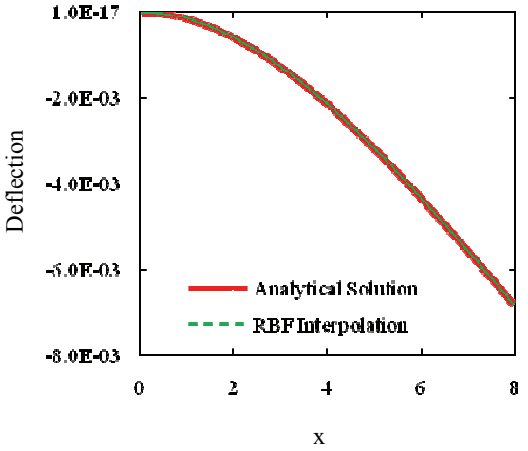

Figure 10: Comparison of the average deflection along the beam (where q=1.03, R=1.25, N_n=450, N_p=1152)

shown in Fig. 11. And, Fig. 13 illustrates that the comparison of stress distributions at one specific point x=4.125. It can be clearly seen that the MPM with the RBF interpolation is far better than element based interpolation schemes for the high accuracy of results, especially in the computation of shear stress. On the other hand, the deflection by either interpolation scheme is nearly identical with the

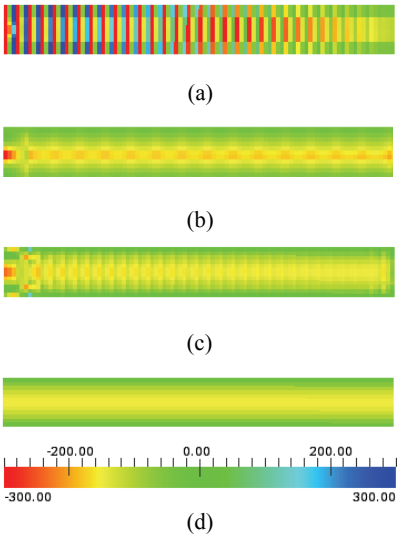

Figure 11: Shear stress distribution computed by (a) Linear interpolation (b) Quadratic interpolation (c) RBF interpolation and (d) Analytical equation

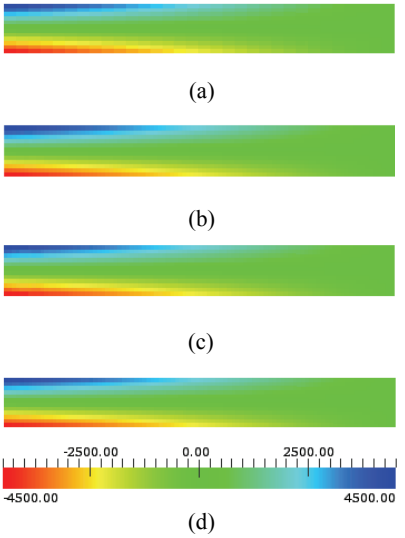

Figure 12: Normal stress distribution computed by (a) Linear interpolation (b) Quadratic interpolation (c) RBF interpolation and (d) Analytical equation

analytical results as shown in Fig. 14.

4.2 Circular disk impact problem

The traditional MPM encounters the computational issues because of the requirement of compatible elements with C^1 continuity condition in the construction of element based shape functions. For instance, the MPM with quadratic interpolation is limited in application [Andersen and Andersen (2010)] and fails to simulate the large deformation case when the material points tend to cross the element boundary.

This circular disk impact case is solved to investigate the capability and performances of the MPM with the RBF interpolation. The energy conservation is examined for convergence to ensure the accuracy of numerical solution. In addition, the material point deformation and their stress distribution are compared with those by the MPM with linear element based interpolation.

The size of 2-dimensional background mesh is (0.5x0.75) and is composed of 150 elements with 176 grid nodes, where the nodal spacing in x and y directions are set 0.05. The two continuum bodies of 0.15 radius circular disk and 0.1 thickness floor are discretized by the 448 and 320 material points, respectively. The material

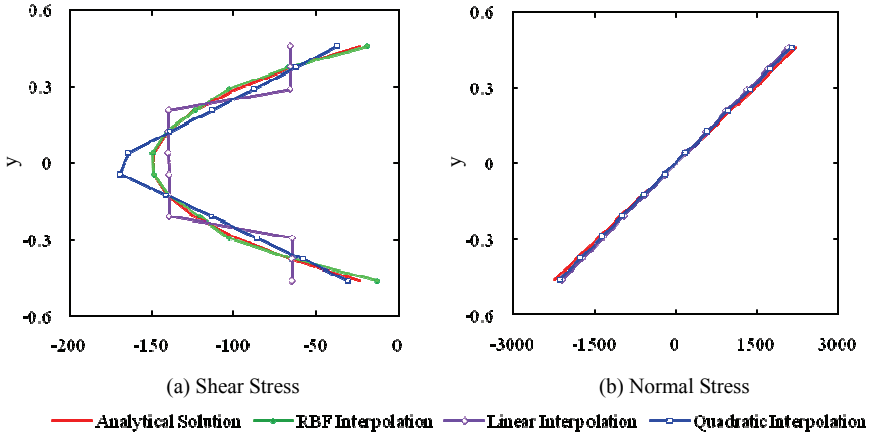

Figure 13: Comparison of (a) shear stress distribution and (b) normal stress distribution @ x=4.125 of the beam (where q=1.03, R=1.25, N_n=238, N_p=1152 for RBF Interpolation)

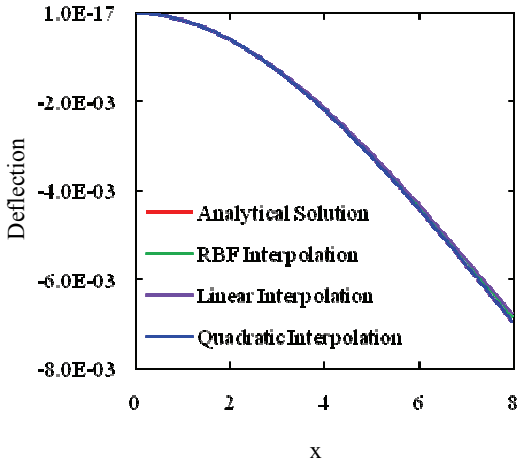

Figure 14: Comparison of the average deflection along the beam (where q=1.03, R=1.25, N_n=238, N_p=1152 for RBF Interpolation)

properties of the circular disk are: Young's modulus(E)=1, Poison's ratio(υ)=0.2 and density (ρ=1), and Young's modulus(E)=10^3, Poison's ratio(υ)=0 and density

(ρ=1000) are applied for the floor. The simulation process is started by applying the initial velocity with the magnitude of (0,-0.2) on the circular disk. The constitutive model of plane stress deformation is used to compute the stress distribution from the strain.

For the shape function calculation, the size of support domain is fixed by setting χ_s =1 instead of χ_s =2 in the previous case of cantilever beam problem. If we select χs =2, the unphysical behavior of the material properties are evolved in the computational process. The reason is the large negative shape function due to the effect of small nodal spacing and the choice of support domain size. Andersen and Andersen (2010) pointed out that the disaster effect of negative shape function value in MPM calculation. However, it remains an open problem to solve in the MPM.

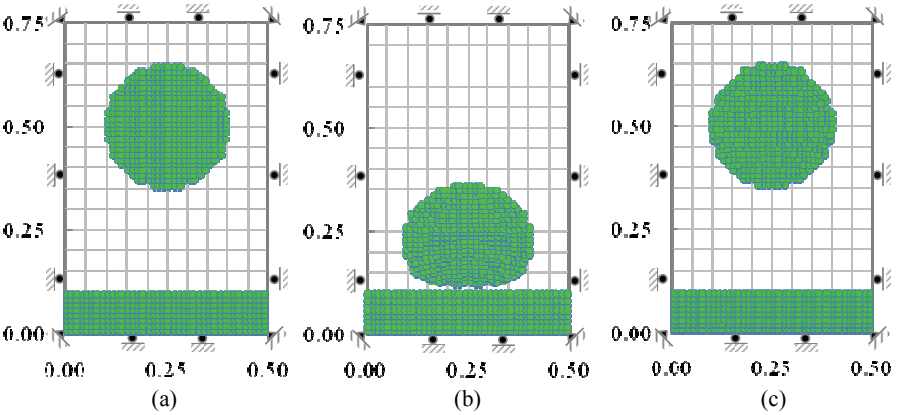

Figure 15: Circular disk position at time (a) t=0 sec (b) t=1.53 sec and, (c) t=3.063 sec

When the support domain size is reduced, fewer nodes are included in the support domain. And, Wang and Liu (2002) recommended to include the polynomial terms in the RBF interpolation. Therefore, the linear polynomial (m=3) is used with the parameters q=1.03 and R= 1.25. Fig. 15 shows the position of the cylinder disk with time t.

Fig. 16 displays the average stress distribution in the cylinder disk during and after impact. In terms of the stress, strain and velocity of material points, total energy is computed by

$$E_{total} = E_{kinetic} + E_{strain} \ , \tag{54}$$

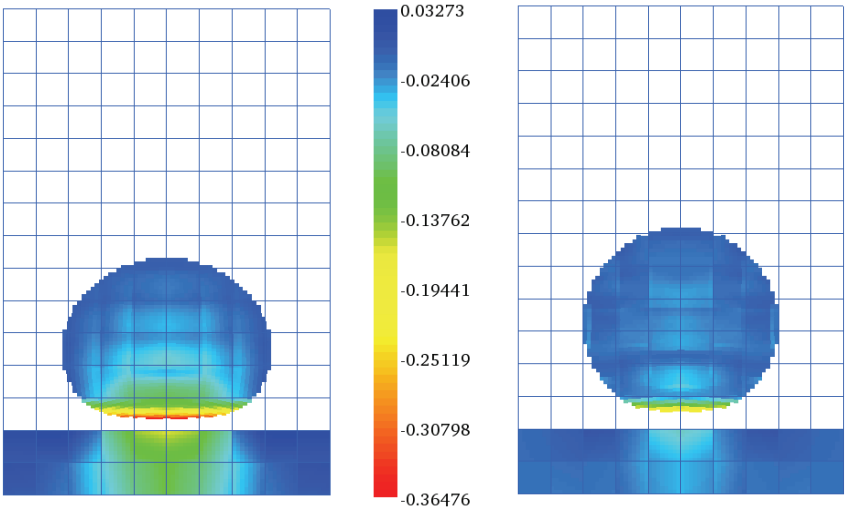

Figure 16: Stress distribution in the material points (a) during impact and (b) after impact

$$E_{kinetic} = \frac{1}{2}\sum_{p=1}^{N_p} m_p\, v_p^2, \tag{55}$$

$$E_{strain}^{t+\Delta t} = E_{strain}^{t} + \sum_{p=1}^{N_p} \mathrm{V}_p^{t+\Delta t}\, \frac{\sigma_p^t + \sigma_p^{t+\Delta t}}{2} : \Delta\varepsilon_p^t, \tag{56}$$

where $\mathrm{V}_p^{t+\Delta t} = J\,\mathrm{V}_p^0$ is the updated volume of any material point and V_p^0 is the initial volume at instant t=0.

Fig. 17 plots the energy distribution of the circular disk and we can find that the energy conserves well on the whole computation process. Finally, Fig. 18 displays the root mean square error (RMSE) between the RBF-based material point positions and their average stress, and the respective results calculated by the MPM with linear interpolation. It is also observed that the differences on the simulation results are tiny and both cases satisfy the energy conservation. However, as mentioned previously, the computational process is broken down when the MPM with quadratic interpolation is tested to this impact problem.

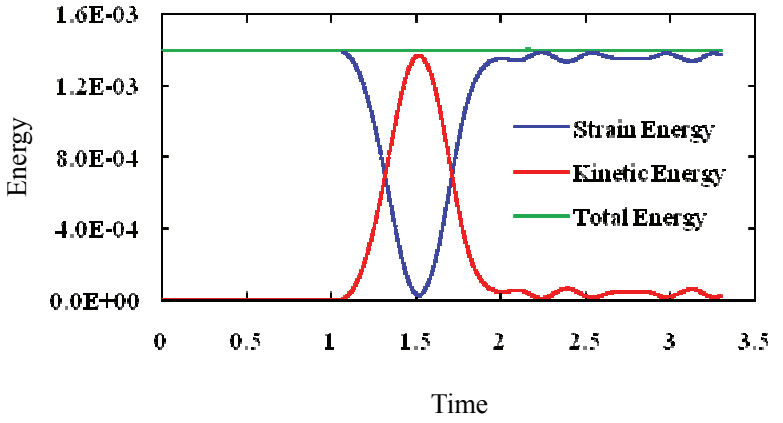

Figure 17: Energy distribution of the circular disk throughout the simulation process

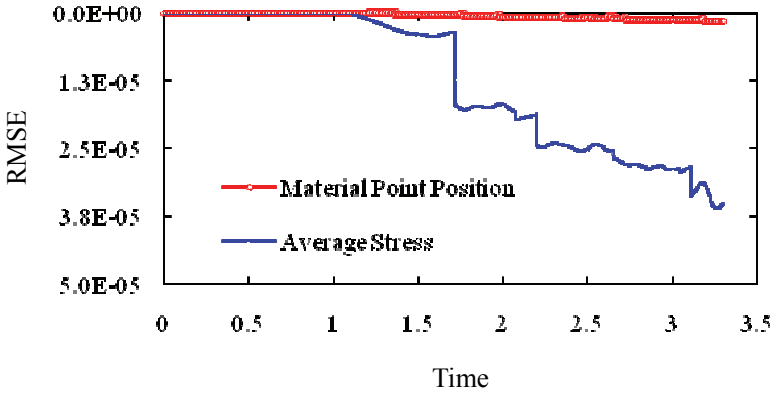

Figure 18: Description of the root mean square error (RMSE) between the simulation results by linear and RBF- interpolation

5 Conclusions

In this study, the RBF interpolation is used to construct the shape function within the MPM framework. Depending on the types of problems, the support domain is selected covering the number of nodes varying from 4∼20. This study also finds that the MQ RBF interpolation with non-integer parameter q has higher degree of

smoothness. This new proposed scheme is successfully implemented to the two different benchmark solid mechanics problems. Numerical experiments show that the RBF-based MPM can produce accurate numerical results and also conserve energy.

It is noted that the traditional MPM with element based shape function can not obtain the accurate solution of shear stress distribution of the cantilever beam. Moreover, the quadratic interpolation is not feasible to the MPM due to the lack of continuity between the elements.

Based on the foregoing numerical results and discussions, it can be concluded that the RBF interpolation yields better accuracy than the traditional element based schemes. The other types of radial basis functions such as Gaussian and Thin Plate Spline can also be used for the construction of the RBF- based MPM scheme. The further work along this line is still under way and will be reported in a subsequent paper.

Acknowledgement: The work described in this paper was supported by the National Basic Research Program of China (973 Project No. 2010CB832702), the Opening Fund of the State Key Laboratory of Structural Analysis for Industrial Equipment (GZ0902), and the R&D Special Fund for Public Welfare Industry (Hydrodynamics, Project No. 201101014).

References

Andersen, S.; Andersen, L. (2010): Analysis of spatial interpolation in the material –point method. *Comput. Struct.*, vol. 88, pp. 506-518.

Bardenhagen, S. G. (2002): Energy conservation error in the material point method for solid mechanics. *J. Comput. Phys.*, vol. 180, pp. 383-403.

Bardenhagen, S. G.; Brackbill, J. U. (1998): Dynamic stress bridging in granular material. *J. Appl. Phys.*, vol. 83, pp. 5732-5740.

Bardenhagen, S. G.; Brackbill, J. U.; Sulsky, D. (2000): The material point method for granular materials. *Comput. Meth. Appl. Mech. Eng.,* vol. 187, pp. 529-541.

Bardenhagen, S. G.; Guilkey, J. E.; Roessig, K. M.; Brackbill, J. U.; Witzel, W. M.; Foster, J. C. (2001): An improved contact algorithm for the material point method and application to stress propagation in granular material. *CMES: Computer Modeling in Engineering & Sciences*, vol. 2, pp. 509-522.

Bardenhagen, S. G.; Kober, E. M. (2004): The generalized interpolation material point method. *CMES: Computer Modeling in Engineering & Sciences*, vol. 5, pp.

477-495.

Beissel, S.; Belytschko, T. (1996): Nodal integration of the element-free Galerkin method. *Comput. Meth. Appl. Mech. Eng.,* vol. 139, pp. 49-74.

Burgess, D.; Sulsky, D.; Brackbill, J. U. (1992): Mass matrix formulation of the FLIP particle-in-cell method. *J. Comput. Phys.*, vol. 103, pp. 1-15.

Buzzi, O.; Pedroso, D. M; Giacomini, A. (2008): Caveats on the implementation of the generalized material point method. *CMES: Computer Modeling in Engineering & Sciences*, vol. 31, no. 2, pp. 85-106.

Chen, J. S.; Yoon, S.; Wu, C. T. (2002): Non-linear version of stabilized conforming nodal integration for Galerkin mesh-free methods. *Int. J. Numer. Meth. Eng.*, vol. 53, pp. 2587-2615.

Chen, W.; Tanaka, M. (2002): A meshless, integration-free, and boundary-only RBF technique, *Comput. Math. Appl.*, vol. 43, pp. 379-391.

Chen, Z.; Brannon, R. (2002): An evaluation of the material point method. *SAND Report*, *Sandia National Laboratories*, pp. 1-46. SAND2002-0482.

Franke, R. (1982): Scattered data interpolation: test of some methods. *Math. Comput.*, vol. 38, no. 157, pp. 181-200.

Golberg, M. A.; Chen, C. S.; Bowman, H.; Power, H. (1998): Some comments on the use of radial basis functions in the dual reciprocity method. *Comput. Mech.*, vol. 21, pp. 141-148.

Harlow, F. H. (1964): The particle-in-cell computing method for fluid dynamics. *Meth. Comput. Phys.*, vol. 3, pp. 319-343.

Kansa, E. J. (1990): A scattered data approximation scheme with application to computational fluid-dynamics - I and II. *Comput. Math. Appl.*, vol. 19, pp. 127-161.

Liu, G. R.; Gu, Y. T. (2001): A local radial point interpolation method (LR-PIM) for free vibration analyses of 2-D solids. *J. Sound Vib.*, vol. 246, no. 1, pp. 29-46.

Ma, S.; Zhang, X. (2007): Material point method for Impact and Explosion Problems. *Comput. Mech.,: Proceedings of the 2007 International Symposium on Computational Mechanics in Beijing,* pp. 156-166.

Ma, X.; Giguere, P. T.; Jayaraman, B.; Zhang, D. Z. (2010): Distribution coefficient algorithm for small mass nodes in material point method. *J. Comput. Phys.*, vol. 229, pp. 7819-7833.

Nairn, J. A. (2003): Material point method calculations with explicit cracks. *CMES: Computer Modeling in Engineering & Sciences*, vol. 4, pp. 649-664.

Steffen, M.; Kirby, R. M.; Berzins, M. (2008): Analysis and reduction of quadra-

ture errors in the material point method (MPM). *Int. J. Numer. Meth. Eng.*, vol. 76, pp. 922-948.

Sulsky, D.; Chen, Z.; Schreyer, H. L. (1994): A particle method for history-dependent materials. *Comput. Meth. Appl. Mech. Eng.,* vol. 118, pp. 179-196.

Sulsky, D.; Schreyer, H. L. (1996): Axisymmetric form of the material point method with applications to upsetting and taylor impact problems. *Comput. Meth. Appl. Mech. Eng.,* vol. 139, pp. 409-429.

Sulsky, D.; Zhou, S. J.; Schreyer, H. L. (1995): Application of a particle-in-cell method to solid mechanics. *Computer Physics Comm.*, vol. 87, pp. 136-252.

Timoshenko, S. P.; Goodier, J. N. (1970): *Theory of elasticity*. 3^{rd} *ed.*, McGraw-Hill, New York.

Wallstedt, P. C.; Guilkey, J. E. (2008): An evaluation of explicit time integration schemes for use with the generalized interpolation material point method. *J. Comput. Phys.*, vol. 227, pp. 9628-9642.

Wang, J. G.; Liu, G. R. (2002): A point interpolation meshless method based on radial basis functions. *Int. J. Numer. Meth. Eng.*, vol. 54, no. 11, pp. 1623-1648.

Wang, J. G.; Liu, G. R. (2002): On the optimal shape parameters of radial basis functions used for 2-D meshless methods. *Comput. Meth. Appl. Mech. Eng.,* vol. 191, no. 23-24, pp. 2611-2630.

Wang, J. G.; Liu, G. R.; Lin, P. (2002): Numerical analysis of Biot's consolidation process by radial point interpolation method. *Int. J. Solids Struct.*, vol. 39, no. 6, pp. 1557-1573.

Wieckowski, Z. (2003): Modelling of silo discharge and filling problems by the material point method. *Task Quarterly*, vol. 4, pp. 701-721.

Wieckowski, Z. (2004): The material point method in large strain engineering problems. *Comput. Meth. Appl. Mech. Eng.,* vol. 193, pp. 4417-4438.

Zhang, X.; Sze, K. Y.; Ma, S. (2006): An explicit material point finite element method for hyper-velocity impact. *Int. J. Numer. Meth. Eng.*, vol. 66, pp. 689-706.